Charge Delocalization through Benzene, Naphthalene, and Anthracene Bridges in π-Conjugated Oligomers: An Experimental and Quantum Chemical Study

Alicia M. Fraind,[†,#] Gjergji Sini,[§,∥] Chad Risko,[§] Lev R. Ryzhkov,[⊥] Jean-Luc Brédas,[§,○] and John D. Tovar*[,†,‡]

[†]Department of Chemistry and [‡]Department of Materials Science and Engineering, Johns Hopkins University, Baltimore, Maryland 21218, United States

[§]School of Chemistry & Biochemistry and Center for Organic Photonics and Electronics, Georgia Institute of Technology, Atlanta, Georgia 30332, United States

[∥]Laboratoire de Physicochimie des Polymères et des Interfaces (LPPI), Université de Cergy-Pontoise, 5 mail Gay-Lussac, F-95031 Cergy-Pontoise Cedex, France

[⊥]Department of Chemistry, Towson University, Towson, Maryland 21252, United States

Ⓢ *Supporting Information*

ABSTRACT: To understand the influence of orthogonal conjugation pathways fused directly to π-conjugated polymer backbones, we synthesized and studied three series of thiophene-based model compounds containing benzene, naphthalene, and anthracene *peri*-substituted central cores as representative acenes. These models were functionalized with methyl groups at the reactive thiophene positions in order to generate and observe oxidized species without complications from follow-up polymerization. The neutral monomers and their oxidized charged counterparts were subjected to cyclic voltammetry, spectroelectrochemistry, and EPR spectroscopy as appropriate, and these results were further corroborated with thorough density functional theory studies. This joint experimental and theoretical analysis allowed us to determine that benzene-based conjugated linkers led to more delocalized charge carriers on account of the quinoidal character maintained within the benzene core. In contrast, anthracene-based linkers displayed very localized carriers due to torsional strain between the adjacent aryl groups and to the local evolution of formal aromatic sextets on the benzo-fused rings orthogonal to the backbone in the quinoidal state. In some cases, the electronics of the thiophene-based substituent dominated the electronic properties of the oxidized species regardless of the nature of the central acene linker. These results highlight the dramatic influence that orthogonal conjugation pathways can exert on the electronic properties of π-conjugated materials.
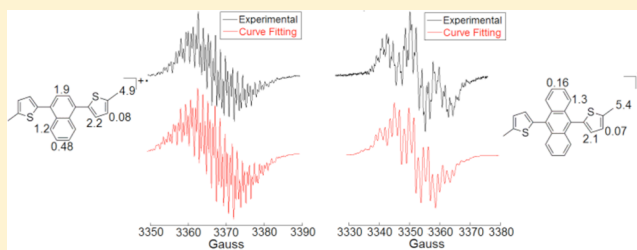
I. INTRODUCTION

Organic π-conjugated polymers show promise for use in a variety of optoelectronic applications. A thorough understanding of the intra- and intermolecular charge transfer processes operative within these polymers and the monomeric repeat units that comprise their conjugated backbones is therefore important in order to understand their underlying physical properties and impact on performance in a device architecture. In general, the oxidation of these systems leads to polymer geometric reorganization and the concurrent formation of a variety of electronic states relevant for charge transport, including spin-bearing radical cations (polarons), spinless dications (bipolarons), and through-space radical cation complexes (π-dimers).[1−3] Although several spectroscopic investigations have been conducted on polymer systems in their neutral and charged states to characterize these relevant intermediates, the experimental results can be difficult to unambiguously interpret, especially for measurements on solid-state materials.[2] For this reason, molecular model compounds have been prepared and investigated. Care must be taken when exploring oxidized molecules due to undesired polymerization; importantly, synthetic procedures that allow for the incorporation of blocking groups at reactive positions can eliminate possibilities for facile follow-up reactions. For example, methyl-blocked oligothiophenes have been used as models for radical cations in the respective polythiophenes,[4−6] and cyclophane structures have been built with cofacial oligothiophenes as model monomers for π dimer structures.[7]

The electronic and geometric structure reorganization is exemplified by a transition from *aromatic* to *quinoidal* bonding

patterns where the localized monomer aromaticity is preserved in the former and broken in the latter to provide a more delocalized structure. Because the aromaticity of the benzenoid components of the polymer repeat units must be disrupted during this process, monomer units with low aromatic stabilization energies have been targeted. Among the primary examples are monomers based on heterocycles such as pyrroles,[8] thiophenes,[9] and, more recently, ethylene dioxythiophenes (EDOTs).[10] This molecular engineering is useful to control the electronic properties along the conjugation pathway of the polymer, but π-electron influences *orthogonal* to the conjugation pathway are also important. Two ways to achieve orthogonal effects are through cruciform-like conjugated structures and through the direct ring fusion of aromatic units onto the polymer backbone. A powerful example of the effects of orthogonal ring fusion and the impacts on the ground-state electronic structure comes from the work of Wudl and co-workers with benzo[*c*]thiophene, where aromaticity preservation in the orthogonal benzene subunit forces the polymer main chain effectively into a quinoidal ground-state configuration.[11]

One can easily make the structural jump to naphthalene and anthracene-based structures where the conjugation pathways through the *peri*-positions (1,4 and 9,10, respectively) might also lead to unusual electronic perturbations that impact energy migration due to the prospects for orthogonal localization of aromaticity in quinoidal structures. While it has been shown that conjugated molecules where ethynyl bridges are linked to anthracene cores can enhance electronic communication,[12] direct diaryl amine links promote distinct mixed-valent character in the associated radical cations[13,14] and *t*-butyl hydrazine substituents as donors allow for the measurement of intramolecular electron transfer rates but do not maintain coplanarity with the central bridges.[15,16] This can also be observed in another sense in extended tetrathiafulvene (exTTF) derivatives where dicationic structures show dramatic localization of aromaticity in the pendant sulfur heterocycles and a concurrent restoration of aromaticity within anthracene,[17] and more recently in differences in molecular scale conduction through different presumably oxidized diamino acenes.[18] These observations are consistent with our recent studies of polymers containing anthracene cores that were studied in the context of understanding how orthogonal ring fusion can impact transport processes in conjugated polymers.[19] Specifically, we found that the anthracene containing polymers had very restricted delocalization as they were oxidized into presumably conductive states. Unfortunately, we were unable to definitively assign the origins of this localization due to the potential contributions of (i) steric clashing and torsional strain serving to frustrate intramolecular planarization (as is coincidentally found in the exTTF dication systems) or (ii) the evolution of aromaticity in the quinoidal electronic structure of the oxidized polymer where π-electrons are "tied up" in peripheral aromatic sextets rather than able to participate in quinoidal delocalization.

We report here a joint theoretical and experimental study to determine the extent of charge delocalization through benzene, naphthalene, and anthracene cores doubly substituted with thiophene and EDOT units as simple models for thiophene-derived conducting polymers containing these hydrocarbon units. A critical component of our work is the use of EPR spectroscopy to understand the extent of spin delocalization on the different acene cores. We find here that EPR is instrumental in the confirmation of radical cation delocalization through the benzene and naphthalene cores compared to the significant localization imposed by the anthracene cores. EPR was further used to elucidate the potential for mixed-valence properties in these model systems.

II. EXPERIMENTAL SECTION

Synthesis. All syntheses were performed on a Schlenk line using standard air-free techniques. Ether and tetrahydrofuran (THF) were distilled from sodium/benzophenone before use. All other reaction solvents were degassed before use. Palladium catalysts were purchased from Strem Chemicals, and all other reagents and chemicals were purchased from Aldrich and used as received. The mono- and disubstituted acene monomers were made using Stille couplings. Prior to the couplings, 2-methylthiophene was stannylated, EDOT was methylated and stannylated, and 2-methylthiophene was brominated and coupled to 2-tributylstannyl thiophene, forming 5-methyl-2,2′-bithiophene which was then stannylated. The stannylated heterocycles were coupled to 1,4-dibromobenzene, 1,4-dibromonaphthalene, 9,10-dibromoanthracene, 1-bromonaphthalene, and 9-bromoanthracene. The synthesis of molecules with deuterated acene cores followed the procedure outlined above while using the respective deuterated dibrominated acene cores. The synthesis of molecules with deuterated methyl groups was carried out by lithiating the parent monomer and quenching the lithiate with deuterated iodomethane. The identities and purities of all compounds were verified by ^{1}H NMR (400 MHz) and ^{13}C NMR (100 MHz) obtained on a Bruker Avance spectrometer. High resolution electron impact/chemical ionization (EI/CI) mass spectrometry was obtained on a VG Instruments VG70S magnetic sector mass spectrometer. Synthesis details and molecular characterization data can be found in the Supporting Information.

Electrochemistry. Methylene chloride (DCM) for electrochemistry was passed through alumina columns and dried over 3 Å sieves. All electrochemical solutions were prepared in anhydrous 0.1 M n-Bu$_4$NPF$_6$ (TBAP) in DCM. Monomer cyclic voltammagrams were obtained using a 2 mm^2 platinum button working electrode with a quasi-internal Ag/Ag$^+$ reference electrode (silver wire immersed in 0.01 M AgNO$_3$ and 0.1 M TBAP in acetonitrile, separated from the cell with a porous Vycor frit, obtained from BioAnalytical Systems) and a platinum wire counter electrode using a scan rate of 100 mV/s. The half-wave potential of the Fc/Fc$^+$ couple was used as an external standard. The potentials were cycled using an Autolab PGSTAT 302 bipotentiostat. Coulometry and spectroelectrochemistry were performed in a BASi spectroelectrochemical quartz thin-layer cell with a 1 mm path length containing a platinum minigrid working electrode, platinum counter electrode, and the Ag/Ag$^+$ reference electrode described above. UV/vis measurements were taken with a Varian Cary 50 Bio UV/vis spectrophotometer.

EPR Spectroscopy. EPR samples were prepared by stirring a solution of monomer in dry, air-free DCM that was passed through alumina columns and was further degassed over calcium sulfate followed by air-free distillation before use during chemical oxidations. Each monomer was stirred with the noted amount of oxidant for 30 min before transferring the sample to an EPR tube fitted with a septum under argon. Samples oxidized with EtO$_3$SbCl$_6$ or p-BrPhNSbCl$_6$ were first stirred with AgClO$_4$ for 15 min to prevent line broadening.[20] EPR spectra were obtained using an X-band Bruker EMX

spectrometer, and the data were analyzed using WinEPR. All simulations (except Figure 6d) were performed using EasySpin, a computational package for spectral simulation and analysis based on the commercial technical computational software package Matlab.[21] The simulation in Figure 6d was performed using WinSim, a program that refines hypothetical simulation parameters to optimal values.[22]

Computations. The geometries of all species in the neutral and radical cation states were optimized without symmetry constraints and followed with frequency calculations to ensure that the optimized structures correspond to minima. For each molecule, different conformers/isomers were considered in order to check for their relative energetic stability. Both density functional theory (DFT), employing a variety of density functionals (B3LYP,[23,24] M06-L,[25] M06-2X,[25] M06-HF[25]), and wave function (AM1, RHF, CISD) methods were used in the study as questions pertaining to the localization/delocalization of the radical cation were addressed. The 6-31G(d,p) basis set was used for all geometry optimizations. The ground-to-excited state transitions for each compound both in the neutral and radical cation state were obtained with time-dependent DFT (TDDFT)[26−30] calculations using the same basis set. In the case of the mTXT compounds, the TDDFT calculations were performed with all the DFT methods. Each system in both states of interest was evaluated both in an isolated ("gas phase", $\varepsilon = 1$) environment and taking into account the dielectric environment provided by dichloromethane (DCM, $\varepsilon = 8.93$), which is the solvent used throughout the experimental work. The conductor-like polarizable continuum model (CPCM[31,32]) was used for the self-consistent reaction field (SCRF) calculations. All results presented below include the dielectric effects.

For each method, charge distributions were evaluated on the basis of the natural population analysis (NPA).[33] The Fermi contact couplings were obtained at the unrestricted B3LYP/6-31G(d,p) level of theory. Calculations with the larger EPR-II and EPR-III basis sets[34] were also performed, though there was no improvement in the agreement with the experimental results. Hyperfine Fermi coupling constant calculations using the PBW91[35,36] functional recommended by Filatov et al.[37] were also performed, though the results showed no general improvement vs B3LYP. The Gaussian 09[38] software suite was used for all calculations.

III. RESULTS AND DISCUSSION

Previously, we studied 1,4-disubstituted benzene and naphthalene as well as 9,10-disubstituted anthracene with electropolymerizable thiophene, ethylene dioxythiophene (EDOT), and bithiophene units.[19] Electrochemical, spectroelectrochemical, UV/vis, and conductivity measurements were used to understand how the electronic properties of the monomer and polymer systems changed with oxidation. Oxidized benzene containing polymers had very delocalized electronic structures, whereas much of the electron localization was relieved upon oxidation of the naphthalene containing polymers. The EDOT-based anthracene monomer was the only anthracene containing monomer that polymerized, and the electron localization pendant to the central charge transport pathway remained even in the oxidized film.

The involvement of the π-electrons of each neutral monomer in the conjugation pathway was inferred from electrochemical and UV/vis studies. A lower electrochemical oxidation potential and longer wavelength UV/vis absorption should suggest greater electron delocalization; however, the absorption spectra of the oxidized monomers could not be recorded because of their facile subsequent polymerization. Futhermore, the electropolymerized materials have relatively poorly defined structure both in terms of polymer length and in terms of intermolecular stacking/aggregation in the electrode modified films. We report here the synthesis of well-defined model monomers with methyl groups in the α-thienyl positions to block polymerization and allow the electron density distribution of the resulting radical cations to be determined (Chart 1).

Chart 1. Monomers with Benzene, Naphthalene, and Anthracene Cores Synthesized by Stille Couplings

The general extent of electron delocalization was elucidated from electrochemical, coulometry, and theoretical studies before the electron density of the radical cation at each spin bearing atom was measured by EPR spectroscopy.

A. Electronic Structure and Optical Properties of the Neutral State. We start our discussion with the theoretical description of the neutral ground states. Select geometric parameters for the neutral states [both in the gas phase and in an implicit solvent dielectric medium ($\varepsilon = 8.93$, dichloromethane)] as determined at the B3LYP/6-31G(d,p) level of theory are provided in the Supporting Information (Figure S1). One of the integral geometric parameters to follow on going from the neutral to radical cation states is the dihedral angle between the central acene unit and the thiophene-based substituent. In agreement with previous results,[14] the dihedral angles between the acene bridge and the adjacent thiophene rings in the mTXT series (in the effective dielectric medium) increase from benzene (21.9°) to naphthalene (44.8°) to anthracene (89.9°). Similar trends are observed for the mEXE and mBXB compounds. These trends are in good accord with the expected increase in steric hindrance between the bridge and the adjacent thiophene rings in the order benzene < naphthalene < anthracene.

Figure 1 provides illustrations of select frontier molecular orbitals of the mTXT series; similar illustrations for the remaining molecules can be found in the Supporting Information (Figures S2, S3, and S4). With the exception of mTAT, the HOMOs are delocalized over the entirety of the
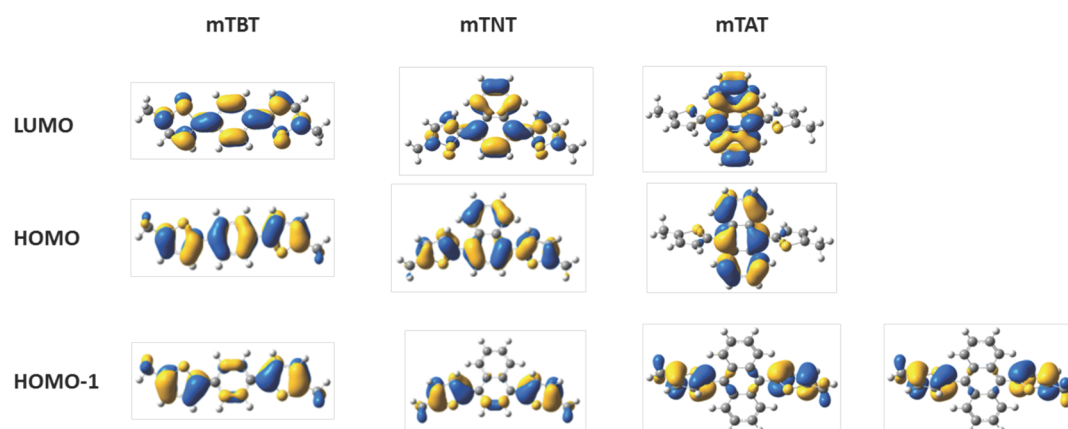
Figure 1. Illustrations of select frontier molecular orbitals as determined at the CPCM/B3LYP/6-31G(d,p) level of theory. Note that the HOMO-1 and HOMO-2 of mTAT are degenerate. (See Figure S2 in the Supporting Information for a selected set of frontier molecular orbitals for the entire molecular series.)

molecular structures, while the HOMO-1 is mostly localized on the respective end groups (with little to no wave function on the acene bridge); the wave functions on the end groups in the HOMO and HOMO-1 are the bonding (plus)/antibonding (minus) combinations of the (isolated) end group HOMOs. The situation differs for mTAT, however, as the HOMO is anthracene (bridge) localized; the HOMO-1 and HOMO-2 are degenerate bonding/antibonding combinations of the (isolated) thiophene HOMOs, and contain minimal bridge character.

The noted difference of mTAT with respect to the other systems can be realized through inspection of a simple molecular orbital diagram. The left side of Figure 2 shows
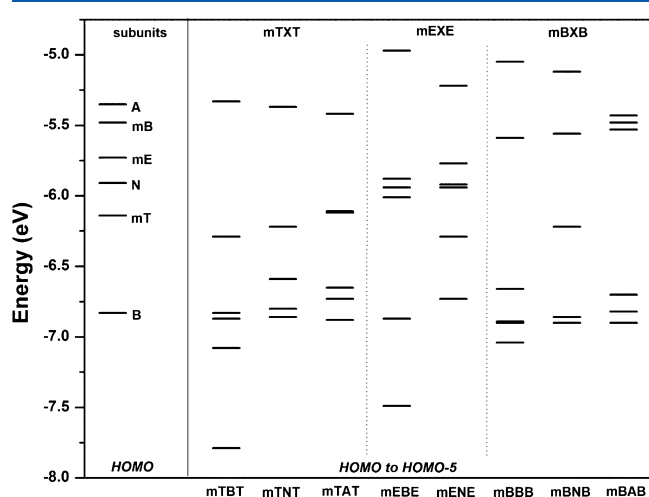

Figure 2. Molecular orbital diagram that includes the HOMO energies of the subunits comprising the full molecules and the HOMO through HOMO-5 energies of the mTXT, mEXE, and mBXB series as determined at the CPCM/B3LYP/6-31G(d,p) level of theory.

the HOMO energies of the isolated acene bridges and end groups, while the right three quadrants show the HOMO through HOMO-5 energies of the three sets of molecular structures. For the systems containing the benzene and naphthalene bridges, there is a relatively large splitting (on the order of 0.4−1.0 eV) between the HOMO and HOMO-1, indicative of fairly strong coupling between the end groups through the bridges. For mTAT, the energy of the bridge-

localized HOMO (−5.42 eV) is very similar to that for isolated anthracene (−5.35 eV), while the energies of the degenerate HOMO-1 and HOMO-2 (−6.11 eV) are similar to that of the isolated methyl-thiophene (−6.14 eV). Interestingly, the energetic splitting between the HOMO through HOMO-2 of mBAB (0.1 eV) is very small, as the three orbitals are nearly iso-energetic. These results show the delicate interplay between geometric structure (e.g., the dihedral angle between the bridge and end groups) and the energetic alignment of the substituents that make up the total molecular structure to the HOMO energies and wave function distributions of the molecules in this series.

UV/vis spectroscopy, combined with detailed insight into the nature of the vertical excitations provided by time-dependent DFT (TDDFT) calculations, was employed as a means to verify these noted differences in the electronic structure. Table 1 shows the observed peak positions of the main UV/vis absorption features (Figure 3) along with the vertical transition energies, oscillator strengths, and electronic configurations for select electronic excitations as determined with TDDFT at the B3LYP/6-31G(d,p) level of theory. The TDDFT calculations on the full molecules reveal that the $S_1 \leftarrow S_0$ transitions across the molecular series can principally be described as HOMO → LUMO one-electron excitations; we note that the $S_1 \leftarrow S_0$ vertical transition energies follow the empirical trends, though they are red-shifted with respect to experiment (Table 1).

The lowest energy UV/vis absorption peaks for mTBT (342 nm, 3.63 eV) and mTNT (344 nm, 3.60 eV) are very similar, indicating that the benzene and naphthalene cores behave in a comparable manner. The mTAT spectrum, however, has vibronic peaks that are reminiscent of, and only slightly red-shifted to, those seen for unsubstituted anthracene (364, 383, and 403 nm for mTAT compared to 340, 360, and 380 nm for anthracene). This suggests minimal interaction between the anthracene core and the heterocyclic substituents. The trends seen for the mTXT monomers are continued in the mBXB series. Although the peaks overlap, the lowest energy transition for mBBB (397 nm, 3.12 eV) is at a shorter wavelength than mBNB (370 nm, 3.35 eV). Neutral mBAB has a series of vibronic features at nearly identical positions to those seen for mTAT, again suggesting that the anthracene is more electroni-cally "isolated" from the heterocycle substituents. The mEXE neutral UV/vis features follow those of the mTXT and mBXB systems, as the lowest energy peaks are at similar positions (357

Table 1. UV/vis Absorption of Neutral Species and TDDFT-Derived (CPCM/B3LYP/6-31G(d,p) Level) $S_0 \rightarrow S_1$ Vertical Transition Energies (eV) and Wavelengths, Oscillator Strengths, and Electronic Configurations Describing the Transition

| | Exp. | TDDFT | | | |
	λ_{max} (nm)	E_{vert} (eV)	λ_{vert} (nm)	f	electronic configuration
			mTX		
mTN	318	3.75	331	0.365	HOMO → LUMO (0.70)
mTA	387, 371, 358, 258	3.14	394	0.151	HOMO → LUMO (0.70)
			mBX		
mBN	342	3.22	385	0.871	HOMO → LUMO (0.70)
mBA	390, 369, 349, 324, 257	2.98 ($S_0 \rightarrow S_1$)	416	0.088	HOMO → LUMO (0.60); HOMO-1 → LUMO (0.36)
		3.16 ($S_0 \rightarrow S_2$)	393	0.167	HOMO-1 → LUMO (0.60); HOMO → LUMO (0.35)
			mTXT		
mTBT	344	3.37	368	1.374	HOMO → LUMO (0.70)
mTNT	342	3.26	380	0.837	HOMO → LUMO (0.70)
mTAT	403, 383, 364, 261	3.01	412	0.296	HOMO → LUMO (0.70)
			mEXE		
mEBE	357	3.27	379	1.277	HOMO → LUMO (0.70)
mENE	365	3.22	385	0.591	HOMO → LUMO (0.70)
			mBXB		
mBBB	397, 222	2.72	455	1.960	HOMO → LUMO (0.70)
mBNB	370	2.78	446	1.426	HOMO → LUMO (0.70)
mBAB	402, 382, 324, 255	2.87 ($S_0 \rightarrow S_1$)	432	0.074	HOMO-2 → LUMO (0.37); HOMO → LUMO (0.60)
		3.04 ($S_0 \rightarrow S_2$)	408	0.401	HOMO-2 → LUMO (0.59); HOMO → LUMO (0.36)
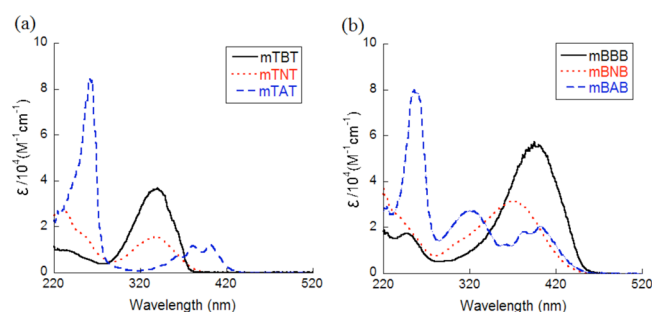
Figure 3. UV/vis spectra of neutral (a) mTXT compounds and (b) mBXB compounds taken from a 0.25 mM solution of the respective monomers in 0.1 M TBAP/DCM.

nm for mEBE and 365 nm for mENE) (Figure S5, Supporting Information).

As a means to further confirm these results empirically, we synthesized monosubstituted methyl blocked thiophene and bithiophene naphthalene (mTN and mBN, respectively) and anthracene monomers (mTA and mBA, respectively). We note that mTN and mBN could not be isolated in an analytically

pure form (~5% impurity); however, we were able to still deduce information from their UV/vis spectra. The UV/vis peaks for the naphthalene-based monomers differ slightly (≈0.3 eV) for both the mTN/mTNT and mBN/mBNB pairs, with the monosubstituted system having a higher energy transition (Figure S6, Supporting Information). This result indicates a potential loss in the length of the conjugation as the naphthyl core loses one of the appended heterocycles. This conclusion is also supported by the shape of the frontier molecular orbital (Figure 1), showing extension of the π-conjugation over both thienyl substituents. For the anthracene containing structures, there is a good deal of similarity among the transition energies of the mono- and disubstituted structures, with the energy difference being ≈0.1 eV, confirming that the π-electrons in the neutral mTAT are not effectively conjugated through the 9- and 10-positions of the anthracene core (as suggested by the localized HOMO depicted in Figure 1). In addition, the vibronic structure reminiscent of isolated anthracene is observed in both the monosubstituted structures, again suggesting excited state localization on the carbocyclic core as in the fully disubstituted structures. As with the disubstituted structures, the TDDFT results provide similar trends regarding
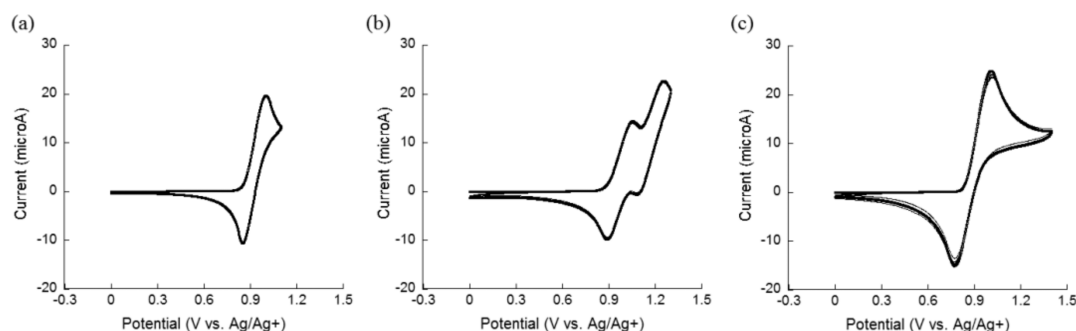
Figure 4. Monomer CV profiles of (a) mTBT, (b) mTNT, and (c) mTAT recorded at a 2 mm² Pt button working electrode; the first scan is bolded. All spectra were obtained from 2.5 mM solutions of monomer in 0.1 M TBAP/DCM using a 100 mV/s scan rate. The $E_{1/2}$ for Fc/Fc⁺ as a reference (averaged from the three profiles) was determined to be 0.239 V under the same conditions.

the transition energies of the monosubstituted systems. In general, the excellent agreement between the UV/vis absorption and TDDFT give credence to the nature of the molecular orbital wave functions described above and provide initial insight into what might be expected in terms of charge (de)localization in the radical cation states.

B. Electrochemical Oxidation and Properties of the Radical Cation State. Cyclic voltammetry (CV) was used to determine the oxidation potentials of the monomer series. As noted above, the presence of the terminal methyl groups at the reactive α-thienyl sites prevents polymerization upon electrochemical oxidation of the monomers. The shapes of the CV traces look quite different for each of the mTXT monomers (Figure 4). The mTNT monomer has two quasi reversible anodic peaks at very close potentials, whereas the CVs of the mTBT and mTAT monomers are reversible, showing the creation of stable radical cations as the monomers are oxidized. The half-wave potentials ($E_{1/2}$) corresponding to the first reversible anodic oxidation processes of the mTXT monomers are very similar, suggesting that the added π-electrons in the naphthalene- and anthracene-based monomers do not facilitate the formation of the oxidized species (Table 2). For the mTX

Table 2. Electrochemical Oxidation Potentials and DFT-Derived (B3LYP/6-31G(d,p)) Vertical and Adiabatic Ionization Potentials (VIP and AIP, Respectively)[a]

	$E_{onset,m}$ (V)	$E_{peak,m}$ (V)	$E_{1/2}$ (V)	VIP[b] (eV)	AIP[b] (eV)
			mTX		
mTN	1.1	1.4	N/A	6.99 (5.64)	6.79 (5.44)
mTA	0.82	1.0	N/A	6.49 (5.44)	6.20 (5.22)
			mBX		
mBN	0.82	1.1	0.96	6.52 (5.32)	6.34 (5.14)
mBA	0.73	0.95	N/A	6.49 (5.38)	6.20 (5.09)
			mTXT		
mTBT	0.80	0.98	0.92	6.61 (5.38)	6.39 (5.17)
mTNT	0.81, 1.1	1.0, 1.2	0.97, 1.12	6.55 (5.39)	6.32 (5.16)
mTAT	0.80	1.0	0.89	6.60 (5.45)	6.27 (5.17)
			mEXE		
mEBE	0.48	0.66	0.61	6.02 (5.00)	5.82 (4.82)
mENE	0.62	1.3	0.87	6.17 (5.24)	5.81 (4.97)
			mBXB		
mBBB	0.70, 0.82	0.75, 1.1	N/A	6.05 (5.06)	5.86 (4.89)
mBNB	0.71	0.96	0.84	6.06 (5.12)	5.88 (4.94)
mBAB	0.62	0.90	0.76	6.33 (5.51)	5.97 (5.05)

[a]All electrochemical data are versus an Ag/Ag$^+$ reference electrode. [b]VIP and AIP data in parentheses were determined using the conductor-like polarizable continuum model (CPCM) taking into account the influence of the dichloromethane (ε = 8.93) environment in the electrochemical measurements.

series, we note some additional changes (Figure S7, Supporting Information). Compared to mTNT, the monosubstituted mTN compound only undergoes one redox process with a similar peak position to the second oxidation of mTNT; however, the mTN oxidation is not electrochemically reversible. Similar trends are observed when mTA and mTAT are compared. The similar oxidation potentials for the mono- and disubstituted naphthalene and anthracene systems suggest that extended π-electron delocalization in the neutral monomers is hindered by these acene cores.

The reversible CVs for mBNB and mBAB are difficult to compare with the mBBB CV, as the latter spectrum contains a

prepeak that decreases in intensity while a peak at higher potentials increases (Figure S8, Supporting Information). Both mBBB peaks are quasi-reversible, whereas the mBNB and mBAB CVs are reversible. Unexpectedly, the $E_{1/2}$ of mBAB is 80 mV less positive than mBNB; however, a full interpretation of these results is hindered by the very low solubility of mBBB (which may influence the CV). With regard to the monosubstituted mBN and mBA systems, mBN has an $E_{1/2}$ that is 12 mV more positive than mBNB (Figure S9, Supporting Information), and the mBA monomer is more difficult to oxidize than mBAB (0.95 and 0.90 V, respectively, Figure S9, Supporting Information). Compared to their disubstituted counterparts, the mBN redox process remains electrochemically reversible while the mBA system is not. For the EDOT systems, the oxidation onset of mENE is significantly higher than that of mEBE (0.62 and 0.48 V, respectively, Figure S10, Supporting Information). The larger differences in mEXE oxidation peak onsets and peak positions compared to those for mTXT may suggest that the π-electrons in the mENE acene core would be more localized than those in mTNT versus their benzene counterparts.

Table 2 also provides the vertical and adiabatic ionization potentials (VIP and AIP, respectively) calculated with and without (e.g., gas phase) the dielectric continuum (ε = 8.93). In the mTXT series, the AIP decreases by about 0.1 eV on going from the benzene to the anthracene bridge for the isolated molecules, a trend that differs slightly from the Koopmans type estimate of the IP using the HOMO energies. However, these changes are completely mitigated when the dielectric continuum model is used, indicating that the ionization potentials for these three molecules in solution are very similar. It is interesting to recall, however, that we expect the oxidation processes to be different in the three molecules, with the resulting charge being relatively delocalized for mTBT and mTNT, while mostly bridge localized in mTAT (as a function of the HOMO wave function (de)localization).

On oxidation, the geometric structures across the three molecular series undergo considerable change, with one of the most notable changes being a decrease in the torsion angle between the external thiophene-based rings and the central acene units.[39] This torsion decreases substantially, moving the molecular structures toward a more coplanar configuration. Specifically, in the mTXT series, the trend still increases from benzene (0.0°) to naphthalene (28.0°) through anthracene (55.9°). These relaxations along the radical cation potential energy surface are on the order of 0.2−0.3 eV in the mTXT series, with the relaxation energy increasing on going from benzene to naphthalene through anthracene. Similar trends are observed in the mEXE and mBXB structures.

To further understand the nature of the radical cation state, it is also of interest to evaluate how the charge (de)localizes as a function of changing the bridge and end groups. On the basis of the UB3LYP/6-31G(d,p) optimizations of the radical cation state, natural population analysis (NPA) was carried out to evaluate the charge distribution (Table 3). The charge distributions follow relatively well the HOMO distributions for the full molecular structures and the HOMO energies (or ionization potential, assuming Koopmans' theorem) of the isolated subunits. There is a fairly well delocalized charge distribution for the benzene and naphthalene bridged systems and a larger degree of charge localization on the bridge of the anthracene-based structures. There is also a noted shift of the positive charge toward the bithiophene groups of the mBXB

Table 3. Natural Population Analysis (NPA) Charge Distribution Obtained at the CPCM/UB3LYP/6-31G(d,p) Level of Theory

	q (mT/mE/mB)	q (bridge)
	mTX	
mTN	0.46	0.54
mTA	0.24	0.76
	mBX	
mBN	0.73	0.27
mBA	0.49	0.51
	mTXT	
mTBT	0.38	0.24
mTNT	0.31	0.38
mTAT	0.19	0.62
	mEXE	
mEBE	0.38	0.24
mENE	0.30	0.40
	mBXB	
mBBB	0.42	0.16
mBNB	0.38	0.24
mBAB	0.29	0.42

Table 4. UV/vis Absorption of the Oxidized Species

	UV/vis		
	coulometry	chemical oxidation	
	λ_{max} (nm)	oxidant	radical species λ_{max} (nm)
	mTX		
mTN	720−477, 440, 318	N/A	N/A
mTA	450	N/A	N/A
	mBX		
mBN	>900, 518, 610	N/A	N/A
mBA	627 (sh), 568	N/A	N/A
	mTXT		
mTBT	>900, 719, 554, 505	EtO$_3$SbCl$_6$	560, 508
		p-BrPhNSbCl$_6$, NOBF$_4$	>900, 560, 508
mTNT	>900, 610, 560 (sh)	EtO$_3$SbCl$_6$	>950, 612
mTAT	462, 299	p-BrPhNSbCl$_6$	720 (sh), 560 (sh), 505, 458
	mEXE		
mEBE	598 (sh), 567	EtO$_3$SbCl$_6$	619, 567
mENE	>950, 635, 547 (sh)	EtO$_3$SbCl$_6$	>950, 634, 550 (sh)
	mBXB		
mBBB	879, 539	EtO$_3$SbCl$_6$	693, 523
mBNB	875, 518	NOBF$_4$	>950, 785 (sh), 678
mBAB	698, 521, 443	p-BrPhNSbCl$_6$	723, 673

systems vs the mTXT systems, as the ionization potential of bithiophene is substantially smaller than that of monothiophene.

For additional experimental insight, standard coulometry was used for bulk electrolysis of the monomer solutions in a spectroelectrochemical cell.[40] In this technique, the solutions were held at a series of potentials for 100 s, starting at a potential where no oxidation occurred and stepping gradually to progressively more positive applied potentials that ultimately resulted in the oxidation of the monomers. UV/vis spectra were recorded at these periodic potentials in order to investigate the optical properties of the charged species (Figure 5 and Table 4). The UV/vis spectra of the oxidized structures are difficult to interpret because oxidation does not lead solely to the creation of radical cations but rather to a proposed mixture of these species with π-dimers and dications.

Despite the complex spectra, several trends are apparent. In mTBT, a set of peaks first grow in at 505 and 554 nm, but these peaks decrease as two longer wavelength peaks (719 nm, >900 nm) are formed. The peak at >900 nm is analogous to the lower energy bipolaron-like structures that appear in conjugated

polymers with high levels of oxidation;[3] however, a second oxidation peak is not seen in the CV. The oxidation of mTNT provides a peak at a longer wavelength than many of those seen for mTBT (610 nm for mTNT compared to 505 and 554 nm for mTBT), suggesting that the change in the conjugation/delocalization efficiency of the oxidized species after oxidation is more important for mTNT than for mTBT.[41] However, mTBT shows an additional broad weak low energy absorption centered at 719 nm. The broad character suggests different conjugation lengths consistent with longer ECLs, whereas the fine structure evident in oxidized mTNT (between 520 and 720 nm) may indicate a more localized electronic structure. The mTNT peaks begin to decrease as a combination of a longer wavelength peak (λ_{max} >950 nm) and shorter wavelength
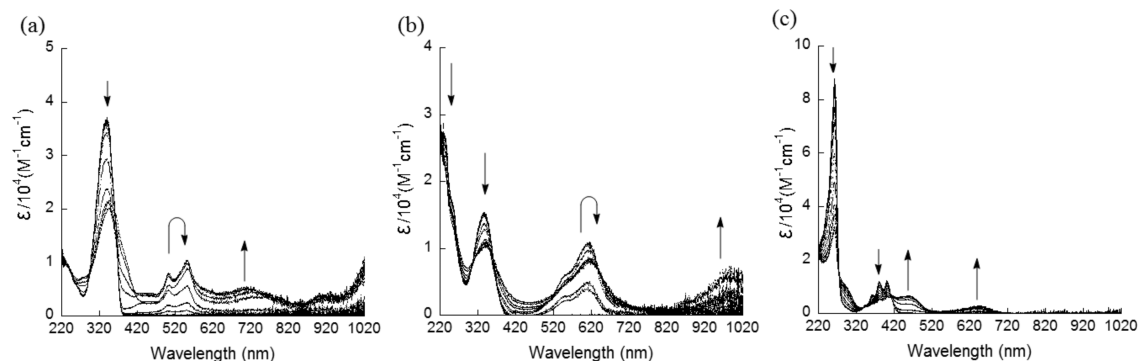

Figure 5. UV/vis spectra from coulometry showing the oxidation of (a) mTBT where the potential was stepped every 100 s in 0.1 V increments between 0.2 and 1.1 V (the first evidence of oxidation occurs at 0.8 V); (b) mTNT where the potential was stepped every 100 s in 0.2 V increments between 0.25 and 0.65 V followed by 0.1 V increments from 0.65 to 1.35 V (the first evidence of oxidation occurs at 1.05 V); and (c) mTAT where the potential was stepped every 100 s in 0.14 V increments between 0.14 and 1.4 V (the first evidence of oxidation occurs at 0.98 V). All spectra were taken using a platinum wire mesh electrode and a 0.25 mM solution of monomer in 0.1 M TBAP/DCM.

G

dx.doi.org/10.1021/jp401448a | J. Phys. Chem. B XXXX, XXX, XXX−XXX

features grew in as oxidation progressed, perhaps due to the creation of another charged species such as a bipolaron. Lastly, in the mTAT monomer, the anthracene vibronic-like structure (261−403 nm) is largely maintained as the monomer is oxidized and much higher energy features evolve during oxidation, suggesting that the anthracene system retains a more electronically localized structure.

Upon oxidation, the mTN monomer behaves differently than mTNT. Although both solutions are the same concentration, the features that grow in with mTN oxidation are much less intense. In addition, the oxidized mTN feature (477−720 nm) is much broader than the shorter wavelength feature seen for oxidized mTNT. The higher wavelength feature (>900 nm) observed during the oxidation of mTNT is absent in the case of mTN (Table 4 and Figure S11, Supporting Information), suggesting that the near IR peak of the radical cation mTNT (Figure 5 and Table 4) should be assigned to the HOMO-1 → HOMO transition, in good agreement with the TDDFT result (946 nm, Table S1, Supporting Information). This data also suggests that π-electron delocalization suffers in mTN compared to mTNT, as the former monomer lacks an additional thiophene ring over which delocalization would occur. The anthracene vibronic structures remain upon oxidation of mTA, whereas the absorbances are reduced as mTAT is oxidized. In addition, a peak at 450 nm grows in as mTA is oxidized which is also seen in mTAT, but oxidation of the disubstituted monomer provides an additional broad feature at higher wavelengths (centered at 644 nm). The growth of these higher wavelength peaks suggest that a limited amount of charge delocalization can occur through the anthracene of mTA and to a larger but still limited extent in mTAT.

We note that the mBXB series follows a similar trend as the mTXT series. The formation of oxidized quinoidal mBNB encourages some delocalization of the naphthalene electrons as seen from the nearly identical UV/vis features (539 and 879 nm for mBBB, 518 and 875 nm for mBNB, Figure S12, Supporting Information). The oxidized mBAB peaks are at considerably shorter wavelengths than those for mBBB and mBNB, again suggesting electron delocalization through the anthracene core is substantially less. Interestingly, the features seen for oxidized mBN are lower in energy than those for mBNB (568, >900 nm for mBN and 518, 875 for mBNB, Figure S13, Supporting Information). Unlike the mTN/mTNT analogues, the presence of a growing peak at the near IR limit of the mBN spectrum (~1020 nm) suggests that the lowest energy peak (875 nm) of the oxidized mBNB spectrum does not correspond to the HOMO-1 → HOMO transition (in the neutral state convention), again in agreement with the TDDFT results (1430 nm for the HOMO-1 → HOMO transition of mBNB, Table S1, Supporting Information). The lack of a large high wavelength feature in the oxidized mBA spectrum, which is present upon mBAB oxidation (centered at 698 nm), suggests that electron delocalization may be even more limited in oxidized mBA compared to mBAB, likely due to the smaller number of aromatic rings available for π-electron delocalization in mBA. The trends for the oxidized mEXE systems more closely resemble those for mTXT, where a substantial blue shift is seen as the acene core is changed from benzene to naphthalene (Figure S14, Supporting Information).

C. Chemical Oxidation and EPR Spectroscopy. Electron paramagnetic resonance has been used previously to study the π-electron distribution of the chemically oxidized 2,5-dimethylthiophene radical cation as well as methyl capped thiophene dimers, trimers, and tetramers, among others.[4−6,42,43] The delocalization observed in 2,5-dimethylthiophene is maintained throughout the series of oligomers, with the largest electron density on the methyl groups due to hyperpolarization from the α-positions of the terminal thiophene rings. There is only a small reduction in the hyperfine splitting (hfs) on the central thiophene ring in methyl blocked terthiophene and no observed hfs reduction on the center quaterthiophene rings. Only a few EPR studies of EDOT containing monomers have been performed; the most pertinent to this research is a study of an ethylenedioxythiophene (EDOT) monomer, dimer, trimer, and tetramer capped with phenyl rings.[44] The large hfs for the monomer and dimer ethylene protons suggests extensive π-electron delocalization through the EDOT cores, but the hfs for the phenyl protons, especially those in the para positions, is much smaller, likely because the acene ring restricted extended delocalization. Oxidation of the EDOT trimer yielded a featureless spectrum.

Chemical oxidations of the monomers were conducted in order to prepare samples for EPR measurements. Chemical oxidation of compounds to form radical cations is not as straightforward as the reduction to form radical anions; therefore, we screened a variety of chemical oxidants. The subtle differences in electronic properties and redox potentials among the monomers studied herein precluded the use of one specific oxidant for all measurements. Each monomer series was treated with different oxidants, and representative spectra were chosen on the basis of sample purity, signal intensity, and hfs resolution. The oxidants used were triethyloxonium hexachloroantimonate (EtO$_3$SbCl$_6$),[45] tris(4-bromophenyl)amminium hexachloroantimonate (p-BrPhNSbCl$_6$),[46] and nitrosonium tetrafluoroborate (NOBF$_4$).[47]

mTBT was treated individually with all three of the chemical oxidants, but we could not convincingly identify the resulting oxidized products. Oxidation of mTBT with EtO$_3$SbCl$_6$ produces a UV/vis spectrum with the two shorter wavelength peak positions (508 and 560 nm) at identical positions to those seen in coulometry (Table 4, Figure S15, Supporting Information). However, no distinct peak at 719 nm or features at higher wavelengths are observed. Chemical oxidation of mTBT with EtO$_3$SbCl$_6$ gives an EPR spectrum that is a mixture of two species, an unexpectedly broad sextet and presumably the desired product (Figure S18, Supporting Information). The chemical oxidation of mTBT with p-BrPhNSbCl$_6$ provides UV/vis peaks at similar positions to those from coulometry, although the intensities of some peaks differ. Lastly, oxidation with NOBF$_4$ gives an oxidized species of mTBT whose UV/vis spectrum looks very structurally similar to the coulometry results, including two peaks 506 and 552 nm as well as a small peak above 900 nm; again, the peak at 719 nm is missing. The EPR spectrum of mTBT treated with p-BrPhNSbCl$_6$ still shows the broad sextet (Figure 6), whereas the oxidation of an mTBT sample with NOBF$_4$ provides an EPR spectrum that is not dominated by a broad sextet but rather contains a large series of narrow lines (Figure S18, Supporting Information). The spectrum is not symmetric and appears to be a mixture of radical containing species: the sextet, the desired product, and a third species.

The excess line width of the sextet lines obtained in the EPR spectra with each oxidant and subsequent lack of further splitting suggest that a dimerized or complexed species has been formed, despite the methyl blocking groups. Dimerization of radical cations, even with methyl blocking groups, is amply
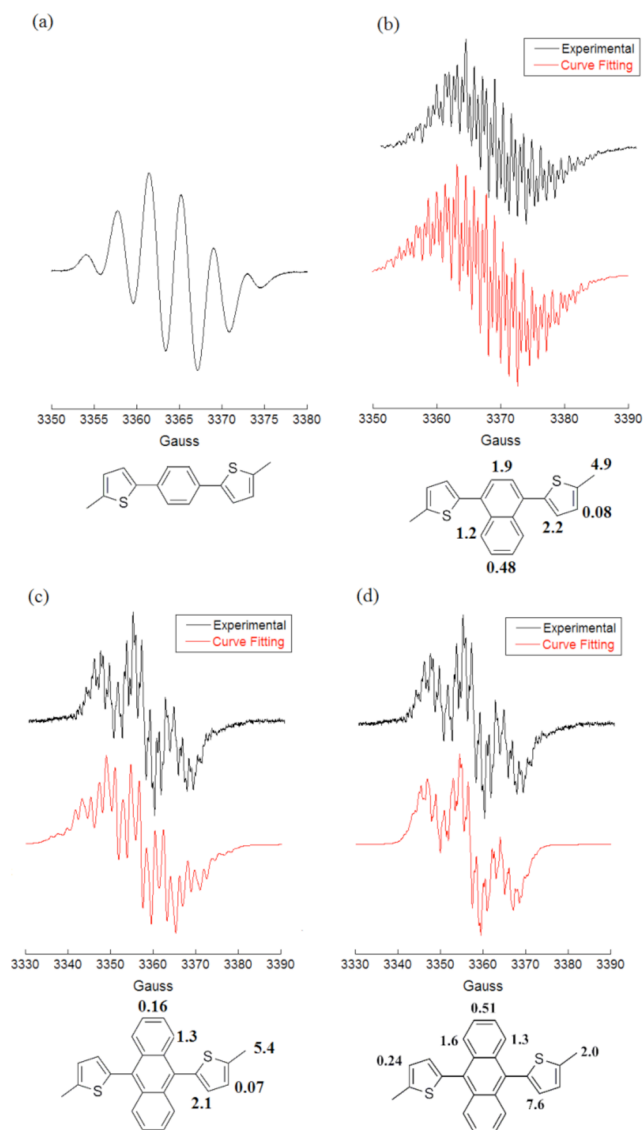
Figure 6. (a) The EPR spectrum of a 20 mM mTBT sample oxidized with 0.5 equiv of *p*-BrPhNSbCl₆; the structure of the neutral monomer is shown below. (b) The EPR spectrum of a 2.5 mM mTNT sample oxidized with 14 equiv of EtO₃SbCl₆, its corresponding simulation, and the assigned hyperfine splitting (in Gauss). (c) The EPR spectrum of a 20 mM mTAT sample oxidized with 0.5 equiv of *p*-BrPhNSbCl₆, its corresponding simulation, and the assigned hyperfine splitting (in Gauss) corresponding to the assignment of the EPR spectrum of mTAT as a septet. (d) Simulation and the assigned hyperfine splitting (in Gauss) corresponding to the assignment of the EPR spectrum of mTAT as a triplet. All spectra were taken in dry DCM.

documented. For example, 2,5-dimethylthiophene has been shown to form a 3,3′-dehydrodimer almost exclusively when oxidized with 4-tolyltitanium(III) bis(trifluoroacetate) in 1,1,1,3,3,3-hexafluoropropan-2-ol.[48] When they are oxidized, radical cations can also form complexes (such as π-dimers). However, it is unlikely that this spectrum is the result of π-dimer formation because the radical cations in a π-dimer complex are spin paired and therefore EPR silent.[49] It is also possible that the oxidant counterion forms a complex with mTBT, leading to the formation of an asymmetric neutral radical which gives a sextet splitting. However, it is worth noting that ROHF calculations also show that symmetry breaking might happen in the case of mTBT in strong polar

solvents (see the Supporting Information for a detailed discussion). On the basis of this assumption, an asymmetric simulation has been performed involving strong hfs values only on five hydrogen atoms, three H on one methyl group and one H on each thiophene (Figure S19, Supporting Information). The simulation in this case is excellent (correlation parameter of 99.9%), but the real nature of this hypothetic asymmetric structure still remains unclear.

With the exception of mTBT, the use of chemical oxidants successfully led to comparable species as those formed electrochemically. The mTNT radical cation is obtained from oxidation with excess EtO₃SbCl₆, leading to a UV/vis spectrum that appears quite similar to the one obtained from coulometry (Table 4). Oxidation of mTNT with EtO₃SbCl₆ provides a radical cation where the largest hfs, and therefore the largest amount of spin density, is found on the methyl groups due to hyperpolarization from the adjacent thiophene carbon atom (Figure 6). The computational results support these assignments, from the good global agreement between the experimental and DFT hfs values (Figure S19, Supporting Information) and from the distribution of the Mulliken spin densities (Figure 7).[50] Similar to other thiophene systems studied by EPR, there is very little spin density associated with the 4-position of the heterocycle but large spin density on the 3-position. A large amount of spin density is also seen in the naphthalene ring; a slightly lower distribution is found on the carbons that are not directly involved in the conjugation pathway, which was expected from the electrochemical data and coulometry.

Chemical oxidation of mTAT with *p*-BrPhNSbCl₆ results in a UV/vis peak around 520 nm with vibronic structure and a longer wavelength shoulder that starts around 620 nm and tails off slowly (Table 4). Chemical and electrochemical oxidation both yield a radical cation with a UV/vis peak around 450 nm; however, a longer wavelength shoulder is seen with the chemical oxidation that may be due to a dication, as no secondary species are seen in the EPR spectrum (Figure S15, Supporting Information). A clean EPR spectrum of the radical cation is obtained when a solution of mTAT is oxidized with about 0.5 equiv of *p*-BrPhNSbCl₆ (Figure 6c,d), although attempts with larger amounts of oxidant led to a presumably dimerized product. At least two different hfs distributions give good computational simulation of the experimental mTAT spectrum. In one simulation, the largest hfs is assigned as a septet (97% correlation) (Figure 6c) but very good correlation (>96%) is also obtained if the largest hfs is arising from a triplet splitting (Figure 6d). This problem frequently arises in systems with complex splitting patterns for which there is little literature precedence. The DFT calculations provide a small hfs value for the methyl hydrogens (2.56 G).

Generally, deuteration is used to identify the atoms responsible for a particular splitting constant because the hfs of deuterium atoms is about 15% that of hydrogen atoms, leading to a reduction of deuterated splitting and overall simplification of the spectrum. A synthetic mTAT variant prepared with perdeuterated methyl groups (Figure 8) gave an EPR spectrum exhibiting a much smaller spectral window (∼1/3 spectrum extent) compared to the non-deuterated one, indicating that the largest hfs values should be assigned to the methyl groups, as with mTNT (Figure S20, Supporting Information). However, the simulation for mTAT shown in Figure 6d, corresponding to a triplet assignment, is also in agreement with the experimental EPR spectra.
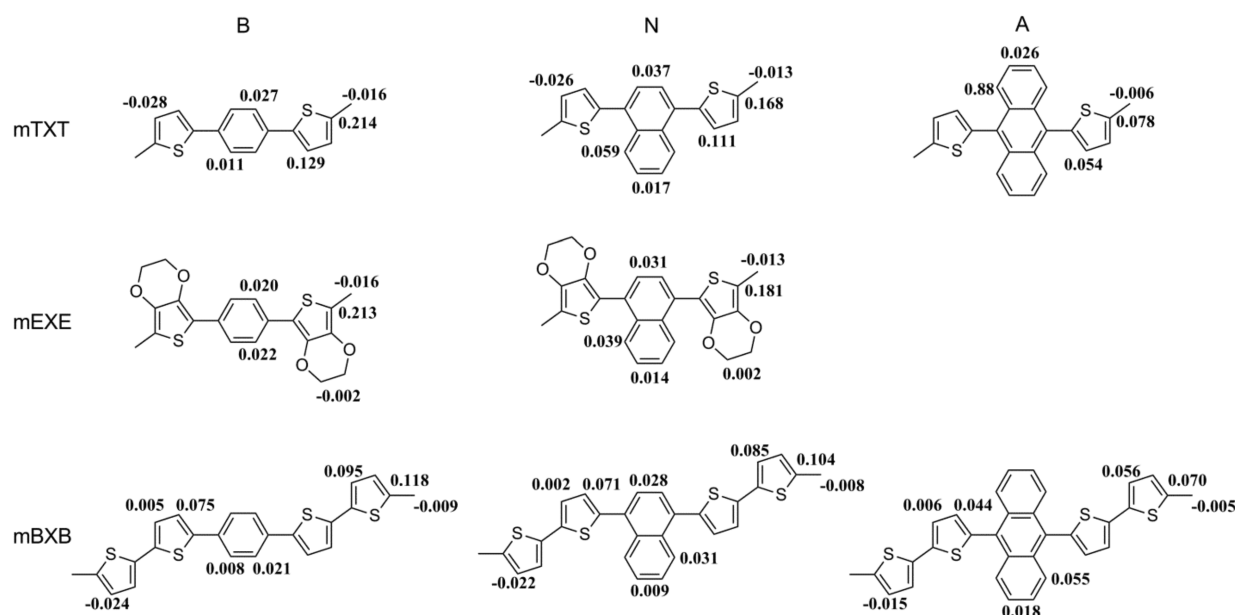
Figure 7. Mulliken spin densities on a selected set of atoms as determined at the CPCM/UB3LYP/6-31G(d,p) level of theory.
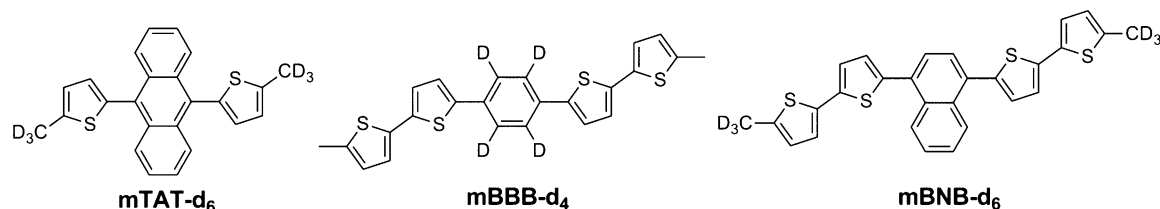

Figure 8. Deuterated compounds synthesized to cross-check the assignment of splitting constants.

The theoretical mTAT spin density distribution shown in Figure 7 indicates that the largest spin density value is found in the anthracene core (thus in the vicinity of the thiophene hydrogens), which seems to be more closely in line with a dominant triplet assignment. Moreover, the spin densities in the thiophene carbon atoms in α-position with respect to the methyl groups decrease in the order mTBT > mTNT > mTAT (0.214, 0.168, and 0.078, respectively), which gives a qualitative indication that the hfs Fermi coupling constants should be smaller in mTAT as compared to mTNT. However, the moderate difference between the spin densities on the anthracene core and on the α-position of the methyl groups (0.088 and 0.078, respectively) along with the DFT hfs values seems to be at odds with the very different hfs values provided by the triplet assignment (7.6 and 2.1 G, respectively). This discrepancy may suggest an insufficient level of theory, which is well-known for the Mulliken spin densities.[43]

The electron density on the thiophene rings does not change much between mTNT and mTAT (in the frame of a septet splitting assignment for the latter). There is limited spin density associated with the 4-positions of the mTAT thiophene rings but large amounts of spin density in the 3-positions. The radical cation distribution on the anthracene ring is markedly different than that on the naphthalene ring. The DFT results indicate that the total spin density localized on the bridge is much greater for mTAT than for mTNT (76 and 44%, respectively, Table 5). The anthracene carbon atoms closer to the 9,10-positions of the ring where the heterocyclic substituents are attached have a significantly larger amount of spin density than those that are off of the main conjugation pathway (Figure 6),

Table 5. Mulliken Spin Densities (%) of Each Fragment, Obtained at the CPCM/UB3LYP/6-31G(d,p) Level

	CH3	Th/EDOT/Th-Th	bridge
		mT*X*T	
mTBT	3	35	24
mTNT	2	26	44
mTAT	1	11	76
		mEXE	
mEBE	2.5	37	21
mENE	2	31	34
		mBXB	
mBBB	2	41	14
mBNB	1.5	36	25
mBAB	1	24	50

suggesting that these last π-electrons remain quite localized in the oxidized species.

Chemical oxidation of mBBB with p-BrPhNSbCl$_6$ gives UV/vis features between 550 and 750 nm, similar to the shortest wavelength feature seen for electrochemically oxidized mBBB, but the longer wavelength feature from coulometry, presumably a dication, is not seen (Table 4, Figure S16, Supporting Information). This oxidant also provides the mBBB EPR spectrum (Figure 9). Oxidation of mBNB with NOBF$_4$ yields a broad UV/vis feature between 550 and 850 nm that encompasses portions of the shorter and longer wavelength peaks seen from electrochemical studies (Table 4). The mBNB EPR spectrum is obtained through oxidation with NOBF$_4$ (Figure 9). Chemical oxidation of mBAB with EtO$_3$SbCl$_6$
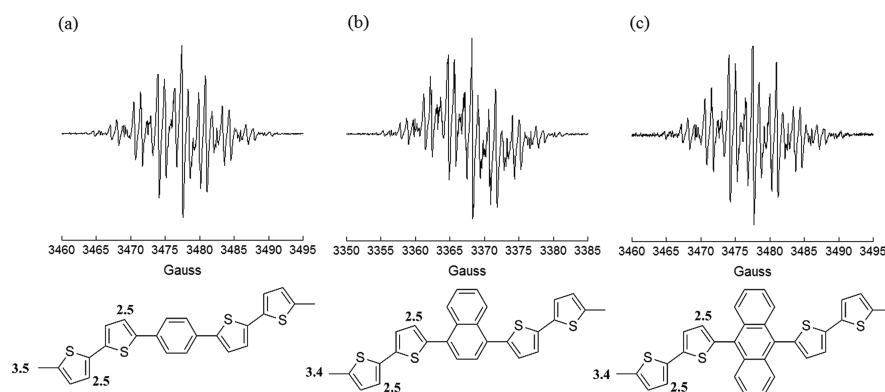
Figure 9. (a) The EPR spectrum of a 1.4 mM mBBB sample oxidized with 0.1 equiv of *p*-BrPhNSbCl$_6$, the assigned hyperfine splitting (in Gauss). (b) The EPR spectrum of a 2 mM mBNB sample oxidized with 1 equiv of NOBF$_4$, the assigned hyperfine splitting (in Gauss). (c) The EPR spectrum of a 10 mM mBAB sample oxidized with 1.5 equiv of EtO$_3$SbCl$_6$, the assigned hyperfine splitting (in Gauss). All spectra were taken in dry DCM.

leads to a UV/vis spectrum that is nearly identical to that seen from coulometry (Table 4); 2 equiv of oxidant can be used to obtain an EPR spectrum.

The EPR spectra of the all the mB*X*B monomers contain a small amount of an unknown radical side product as a result of the oxidation, despite the fact that different oxidants were used for each monomer. The most relevant result is the fact that the mB*X*B EPR spectra are nearly identical. All mB*X*B EPR spectra are septets of quintets, as there are two sets of two hydrogen atoms with almost identical hfs. The smaller hfs seen on the septet of quintets is due to the side product. It was shown by comparison with an mBNB variant with perdeuterated methyl groups that the septet splitting is due to the six hydrogen atoms (Figure S21, Supporting Information) without possibility to predict, with certainty, on which additional atoms the electron density was located. The hydrogen atoms leading to the quintet splitting were expected to be on the acene cores at positions closest to the central conjugation pathway, but comparison with a deuterated benzene variant (Figure S21, Supporting Information) shows that this is not the case. Surprisingly, the EPR spectrum of mBBB with a deuterated benzene core looks identical to that of non-deuterated compound, thus indicating that there is no spin density on these atoms (as well as the naphthalene and anthracene cores). Therefore, the minor splittings of 2.46−2.48 G are assigned to the bithiophene substituents, in the positions shown (Figure 9) as indicated by the DFT results.

The mEBE and mENE radical cations are formed chemically from the addition of EtO$_3$SbCl$_6$, and the resulting UV/vis spectra of the chemically oxidized monomers are very similar to the corresponding spectra obtained from coulometry (Table 4, Figure S17, Supporting Information). The oxidized mEBE EPR spectrum is dominated by a broad septet due to the methyl hydrogen atoms, which is then split by the remaining hydrogen atoms (Figure 10). The mENE EPR spectrum has the same overall appearance as the mEBE spectrum, but the mENE splitting is further split into doublets, likely due to the two naphthalene protons farthest from the main conjugation pathway. This similarity seems to be due to the fact that, in the absence of strong contributions from the EDOT substituents, the methyl groups constitute the principal contributors for the septet splittings observed experimentally in both cases. The slightly larger methyl hfs values for mEBE as compared to mENE (5.8 and 4.9 G, respectively, Figure 10) are
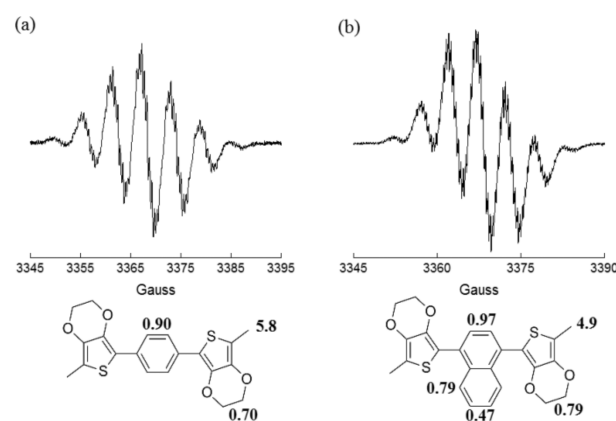

Figure 10. (a) The EPR spectrum of a 20 mM mEBE sample oxidized with 1.5 equiv of EtO$_3$SbCl$_6$, the assigned hyperfine splitting (in Gauss). (b) The EPR spectrum of a 2 mM mENE sample oxidized with 1.5 equiv of EtO$_3$SbCl$_6$, the assigned hyperfine splitting (in Gauss). Both spectra were taken in dry DCM.

in line with the spin densities calculated for the thiophene carbon atoms in the α-position with respect to the methyl groups (0.213 and 0.181, respectively, Figure 7). This assignment is supported by the computations and simulation, which show that there is a smaller amount of electron density on the peripheral atoms of the naphthalene core compared to those closest to the pendant thiophene rings. This suggests that these additional π-electrons in the acene core are somewhat restricted from extended delocalization.

The amount of radical density on the central acene cores is considerably lower in the EDOT systems than it is in the thiophene systems, which agrees with past EPR studies of EDOT containing monomers[42] (see also the total spin density on each fragment, Table 5). The mENE and mTNT spectra exhibit a similar total splitting of ~35 G and are septets, due to the identical dominating hfs values of the methyl groups. The difference between them is due to the additional splitting exerted by the thiophene hydrogen atoms in mTNT. Concerning the hfs values of the atoms closer to the substituents, the lower value in mENE (0.97 G) as compared to mTNT (1.9 G) is due to the lower spin density left for the bridge in mENE (Table 5). This difference may be due to the additional atoms in EDOT fragments compared to thiophenes, thus offering more available space for spin localization in

K

dx.doi.org/10.1021/jp401448a | *J. Phys. Chem. B* XXXX, XXX, XXX−XXX

EDOT, and consequently less contribution from the acene cores. The bridge atoms far from the conjugation pathway are less sensitive to this spin delocalization, as seen from the similar hfs values on these positions (0.48 and 0.47 G for mTNT and mENE, respectively). There is, however, a larger reduction in spin density on the peripheral naphthalene hydrogen atoms versus those closest to the heterocyclic substitutents in mENE compared to mTNT (52 and 75%, respectively).

We finish this section with some considerations regarding charge (de)localization. Delocalization of the radical cation is suggested in all cases from the fact that an equivalent number of hydrogen atoms on both sides of the bridge is necessary to provide a good fit of the EPR spectra via simulation (with the exception being mTBT). Delocalization of the radical cation is also proposed via the DFT calculations. The DFT result, however, is not surprising due to the overdelocalization error known to permeate DFT methods due to the many-electron self-interaction problem; regardless, even for systems in which charge localization is known to occur, previous work has shown that DFT can sufficiently provide average hfs coupling constants and spin distributions.[51]

A charge delocalization scenario in the case of mBXB compounds would require non-negligible hfs values from the bridge, at least for the mBAB compound (Table 5). However, the results concerning the mBXB series are intriguing, as the similar EPR spectra for the three compounds imply a negligible and similar bridge contribution in each case, thus suggesting no localization of the spin density on the benzene, naphthalene, or anthracene cores. The small spin densities calculated on the bridge in the case of mBBB and (to a lesser extent) mBNB (Table 5) seem in line with the experimental conclusion. As for mBAB, strong spin density is still found on the bridge (∼50%), which is incompatible with the EPR silence of the anthracene hydrogens (the same observations could be found on the basis of the DFT hfs values given in Figure S19, Supporting Information). In view of the good overall agreement between the experimental and theoretical results in this study, this last discrepancy points to a charge-localization scenario which, while being out of reach of the DFT methods, is supported by the ROHF results (detailed discussion in the Supporting Information).

CONCLUSIONS

This study has allowed for the interrogation of both neutral and stable oxidized conjugated polymer subunits of well-defined nature. We show that the neutral subunits containing different acenes with different orthogonal conjugation pathways (e.g., 1,4-phenyl-, 1,4-naphthyl-, and 9,10-anthracenyl-) show comparable degrees of electronic delocalization despite the differences in the number of π-electrons contained within these units. Less efficient π-conjugation is found through the anthracene core, which is principally due to the orthogonal ring-to-ring geometry and increased steric hindrance with the substituents. Due to the synthetic design of the monomer units that incorporated methyl-blocking units on the reactive thienyl positions, we were able to more carefully interrogate the spin distributions within oxidized species using spectroelectrochemistry and EPR spectroscopy. These studies clearly show restricted π-electron delocalization within the anthracene-based monomer systems based on the trends in spectral features compared to the respective benzene-based core units. Upon oxidation of compounds containing methyl-blocked thiophene and EDOT, charge delocalization over the entire

molecular backbone is found. The amount of the positive charge localized in the aromatic bridges increases from benzene to anthracene, due to the decreased ionization potential of the aromatic cores. The very small amount of spin density on the peripheral atoms of the naphthalene and anthracene cores suggest that these π-electrons do not participate in the delocalization of the oxidized species.

Interpretation of EPR data supported these findings, although the results were complicated due to the presence of presumed mixed-valence character within bithiophene-based monomers. While a delocalized charge can be inferred from the EPR simulations in the case of mTXT and mEXE series, quite unexpectedly, almost indistinguishable EPR spectra are obtained in the bithiophene-based thienyl monomers, independent of the benzene, naphthalene, or anthracene cores. This last result is interpreted as a strong indication of charge localization on the bithiophene moieties, attributed to the enhanced stability of these units not requiring extended delocalization as a condition for stability/persistence under the reaction conditions.

In total, this joint theory and experimental analysis has provided a fundamental study of the effects of how steric hindrance and orthogonal aromaticity pendant to conjugated polymer main chains can influence charge carrier electronic structures. Given the interest in acene-based organic electronic materials, the monomer analyses presented here provide a suitable foundation for the continued study of extended π-conjugated polymers with similar extents of orthogonal π-electron delocalization arising from complex acene-like aromatic subunits.

■ ASSOCIATED CONTENT

⑤ Supporting Information
Experimental procedures including full characterization for all new compounds, additional UV/vis, CV, and EPR data. TDDFT-derived optical parameters, geometrical parameters for all compounds, frontier molecular orbitals, experimental and theoretical hyperfine coupling constants, geometrical parameters, molecular orbitals, and discussion on symmetry breaking of some radical cation species obtained at the ROHF/6-31G(d,p) level. This material is available free of charge via the Internet at http://pubs.acs.org.

■ AUTHOR INFORMATION

Corresponding Author
*E-mail: tovar@jhu.edu.
Present Addresses
#Department of Chemistry, University of Virginia, Charlottesville, Virginia 22903, United States.
○Also affiliated with the Department of Chemistry, King Abdulaziz University, Jeddah 21589, Saudi Arabia.
Notes
The authors declare no competing financial interest.

■ ACKNOWLEDGMENTS

■ REFERENCES

(1) Brédas, J. L.; Street, G. B. Polarons, Bipolarons, and Solitons in Conducting Polymers. *Acc. Chem. Res.* **1985**, *18*, 309−315.

(2) Miller, L. L.; Mann, K. R. π-Dimers and π-Stacks in Solution and in Conducting Polymers. *Acc. Chem. Res.* **1996**, *29*, 417−423.

(3) Patil, A. O.; Heeger, A. J.; Wudl, F. Optical Properties of Conducting Polymers. *Chem. Rev.* **1988**, *88*, 183−200.

(4) Davies, A. G.; Julia, L.; Yazid, S. N. An Electron Spin Resonance Study of the Radical Cations of Pyrroles, Furans, and Thiophenes in Liquid Solution. *J. Chem. Soc., Perkin Trans. 2* **1989**, 239−244.

(5) Kriste, B.; Tian, P.; Kossmehl, G.; Engelmann, G.; Jugelt, W. EPR Study of Bi-, Ter- and Quaterthiophene Radical Cations. *Magn. Reson. Chem.* **1995**, *33*, 70−76.

(6) Fajarí, Ll.; Brillas, E.; Alemán, C.; Juliá, L. α-Linked Bifuran and α,α'-Linked Tricycles Containing Furan and/or Thiophene. EPR Investigations and Electrochemical Behavior. *J. Org. Chem.* **1998**, *63*, 5324−5331.

(7) Knoblock, K. M.; Silvestri, C. J.; Collard, D. M. Stacked Conjugated Oligomers as Molecular Models to Examine Interchain Interactions in Conjugated Materials. *J. Am. Chem. Soc.* **2006**, *128*, 13680−13681.

(8) Moutet, J.-C.; Deronzier, A. Functionalized Polypyrroles. New Molecular Materials for Electrocatalysis and Related Applications. *Acc. Chem. Res.* **1989**, *22*, 249−255.

(9) Roncali, J. Conjugated Poly(thiophenes): Synthesis, Functionalization, and Applications. *Chem. Rev.* **1992**, *92*, 711−738.

(10) Sotzing, G. A.; Renyolds, J. R.; Steel, P. J. Electrochromic Conducting Polymers via Electrochemical Polymerization of Bis(2-(3,4-ethylenedioxy)thienyl) Monomers. *Chem. Mater.* **1996**, *8*, 882−889.

(11) Wudl, F.; Kobayashi, M.; Heeger, A. J. Poly(isothianaphthene). *J. Org. Chem.* **1984**, *49*, 3382−3384.

(12) Vilà, N.; Zhung, Y.-W.; Henderson, J.; Abruña, H. Anthracene-Bridged Binuclear Ruthenium Complexes: Electrochemical and Spectroscopic Evidence of Electronic Communication through the π-System. *Inorg. Chem.* **2010**, 796−804.

(13) Coropceanu, V.; Malagoli, M.; André, J. M.; Brédas, J. L. Charge-Transfer Transitions in Triarylamine Mixed-Valence Systems: A Joint Density Functional Theory and Vibronic Coupling Study. *J. Am. Chem. Soc.* **2002**, *124*, 10519−10530.

(14) Lambert, C.; Risko, C.; Coropceanu, V.; Schelter, J.; Amthor, S.; Gruhn, N. E.; Durivage, J. C.; Brédas, J. L. Electronic Coupling in Tetraanisylarylenediamine Mixed-Valence Systems: The Interplay Between Bridge Energy and Geometric Factors. *J. Am. Chem. Soc.* **2005**, *127*, 8508−8516.

(15) Nelsen, S. F.; Ismagilov, R. F.; Powell, D. R. Effects of Bridge Redox State Levels on the Electron Transfer and Optical Properties of Intervalence Compounds with Hydrazine Charge-Bearing Units. *J. Am. Chem. Soc.* **1998**, *120*, 1924−1925.

(16) Nelsen, S. F.; Ismagilov, R. F.; Gentile, K. E.; Powell, D. R. Effects of Bridge Redox State Levels on the Electron Transfer and Optical Properties of Intervalence Compounds with Hydrazine Charge-Bearing Units. *J. Am. Chem. Soc.* **1999**, *121*, 7108−7114.

(17) Godbert, N.; Bryce, M. R.; Dahaoui, S.; Batsanov, A. S.; Howard, J. A. K.; Hazendonk, P. Hydroxymethyl-Functionalised 9,10-Bis(1,3-dithiol-2-ylidene)-9,10-dihydroanthracene π-Electron Donors as Synthetic Intermediates for Supramolecular Structures. *Eur. J. Org. Chem.* **2001**, 749−757.

(18) Quinn, J. R.; Foss, F. W., Jr.; Venkataraman, L.; Hybertsen, M. S.; Breslow, R. Single Molecule Junction Conductance through Diaminoacenes. *J. Am. Chem. Soc.* **2007**, *129*, 6714−6715.

(19) Fraind, A. M.; Tovar, J. D. Comparative Survey of Conductive Polymers Containing Benzene, Naphthalene, and Anthracene Cores: Interplay of Localized Aromaticity and Polymer Electronic Structures. *J. Phys. Chem. B* **2010**, *114*, 3104−3116.

(20) Fairhurst, S. A.; Smith, I. M.; Sutcliffe, L. H.; Taylor, S. M. An NMR, ESR, ENDOR, and TRIPLE Resonance Investigation of a Cation Radical Formed from 1,2,4,5-Tetramethoxybenzene. *Org. Magn. Reson.* **1982**, *18*, 231−235.

(21) Stoll, S.; Schweiger, A. Easyspin, a Comprehensive Software Package for Spectral Simulation and Data Analysis in EPR. *J. Magn. Reson.* **2006**, *178*, 42−55.

(22) Duling, D. R. Simulation of Multiple Isotropic Spin-Trap EPR Spectra. *J. Magn. Reson., Ser. B* **1994**, *104*, 105−110.

(23) Becke, A. D. Density-Functional Thermochemistry. III. The Role of Exact Exchange. *J. Chem. Phys.* **1993**, *98*, 5648−5652.

(24) Lee, C. T.; Yang, W. T.; Parr, R. G. Development of the Colle-Salvetti Correlation Energy into a Functional of the Electron Density. *Phys. Rev. B* **1988**, *37*, 785−789.

(25) Zhao, Y.; Truhlar, D. G. Density Functionals with Broad Applicability in Chemistry. *Acc. Chem. Res.* **2008**, *41*, 157−167.

(26) Gross, E. K. U.; Kohn, W. Time-Dependent Density-Functional Theory. *Adv. Quantum Chem.* **1990**, *21*, 255−291.

(27) Gross, E. K. U.; Kohn, W. Local Density-Functional Theory of Frequency-Dependent Linear Response. *Phys. Rev. Lett.* **1985**, *55*, 2850−2852.

(28) Runge, E.; Gross, E. K. U. Density-Functional Theory for Time-Dependent Systems. *Phys. Rev. Lett.* **1984**, *52*, 997−1000.

(29) Bauernschmitt, R.; Ahlrichs, R. Treatment of Electronic Excitations within the Adiabatic Approximation of Time Dependent Density Functional Theory. *Chem. Phys. Lett.* **1996**, *256*, 454−464.

(30) Casida, M. E.; Jamorski, C.; Casida, K. C.; Salahub, D. R. Molecular Excitation Energies to High-Lying Bound States from Time-Dependent Density-Functional Response Theory: Characterization and Correction of the Time-Dependent Local Density Approximation Ionization Threshold. *J. Chem. Phys.* **1998**, *108*, 4439−4450.

(31) Barone, V.; Cossi, M. Quantum Calculaton of Molecular Energies and Energy Gradients in Solution by a Conductor Solvent Model. *J. Phys. Chem. A* **1998**, *102*, 1995−2001.

(32) Cossi, M.; Rega, N.; Scalmani, G.; Barone, V. Energies, Structures, and Electronic Properties of Molecules in Solution with the C-PCM Solvation Model. *J. Comput. Chem.* **2003**, *24*, 669−681.

(33) Reed, A. E.; Weinstock, R. B.; Weinhold, F. Natural Population Analysis. *J. Chem. Phys.* **1985**, *83*, 735−746.

(34) Barone, V. Chapter 8: Structure, Magnetic Properties and Reactivities of Open Shell Species from Density Functional and Self-Consistent Hybrid Methods. In *Recent Advances in Density Functional Methods (Part I)*; Chong, D. P., Ed.; World Scientific Publishing Co. Pte. Ltd.: Singapore, 1995; pp 287−368.

(35) Becke, A. D. Density-Functional Exchange-Energy Approximation with Correct Asymptotic Behavior. *Phys. Rev. A* **1988**, *38*, 3098−3100.

(36) Perdew, J. P.; Wang, Y. Accurate and Simple Analytic Representation of the Electron-Gas Correlation Energy. *Phys. Rev. B* **1992**, *45*, 13244−13249.

(37) Filatov, M.; Cremer, D. Calculation of Spin-Densities within the Context of Density Functional Theory. The Crucial Role of the Correlation Functional. *J. Chem. Phys.* **2005**, *123*, 124101.

(38) Frisch, M. J.; et al. *Gaussian 09*, A.02 ed.; Gaussian, Inc.: Wallingford, CT, 2009 (full reference in the Supporting Information).

(39) As expected, the results obtained at the CPCM/UB3LYP/6-31G(d,p) calculations suggest symmetric geometries and charge distributions both for the neutral and radical cation states. In order to check if symmetry breaking could be found in these radical cations, AM1 and RHF methods were also employed. The results at the UHF level, however, show large degrees of spin contamination. Consequently, restricted open-shell Hartree−Fock (ROHF/6-31G(d,p)) was also employed; symmetric structures were still found for the mTNT, mTAT, and mENE compounds, whereas asymmetric structures were found for mTBT, mEBE, and the complete mB*X*B series. However, ROHF calculations are known to lack electronic correlation, suggesting that based on this frame no clear conclusions on the relative stability of asymmetric versus symmetric geometries could be drawn. What can be retained here is that, if symmetry breaking were to occur in this series, mTBT, mEBE, and mB*X*B would be the most likely candidates for this phenomenon. (A more detailed discussion in this respect is given in the Supporting Information.)

(40) The spectrophotometer employed in the coulometry characterization could not scan the full low-energy portion of the spectrum required to see the low-lying electronic transitions of the radical cation state. TDDFT results for the first transition suggest, using the nomenclature of the neutral species, that the lowest-lying transition is a HOMO-1 → HOMO transition. (Full details of the TDDFT calculations of the radical cation states can be found in the Supporting Information.)

(41) The thiophene-bridge dihedral angles (Supporting Information) provide a possible explanation: while the variation in this dihedral angle is more important for mTBT (∼22° as compared to ∼17° for mTNT), this change takes place near the minimum of the potential surface of mTBT, thus resulting in much smaller energetic effects.

(42) Odom, S. A.; Lancaster, K.; Beverina, L.; Lefler, K. M.; Thompson, N. J.; Coropceanu, V.; Brédas, J. L.; Marder, S. R.; Barlow, S. Bis[bis(4-alkoxyphenyl)amino] of Dithienylethene, Bithiophene, Dithienothiophene and Dithienopyrrole: Palladium-Catalyzed Synthesis and Highly Delocalized Radical Cations. *Chem.—Eur. J.* **2007**, *13*, 9637−9646.

(43) Barlow, S.; Odom, S. A.; Lancaster, K.; Getmanenko, Y. A.; Mason, R.; Coropceanu, V.; Brédas, J. L.; Marder, S. R. Electronic and Optical Properties of 4H-Cyclopenta[2,1-b:3,4-b′]bithiophene Derivatives and Their 4-Heteroatom-Substituted Analogues: A Joint Theoretical and Experimental Comparison. *J. Phys. Chem. B* **2010**, *114*, 14397−14407.

(44) Apperloo, J. J.; Groenendaal, L.; Verheyen, H.; Jayakannan, M.; Janssen, R. A. J.; Dkhissi, A.; Beljonne, D.; Lazzaroni, R.; Brédas, J. L. Optical and Redox Properties of a Series of 3,4-Ethylenedioxythiophene Oligomers. *Chem.—Eur. J.* **2002**, *8*, 2384−2396.

(45) Rathore, R.; Kumar, A. S.; Lindeman, S. V.; Kochi, J. K. Preparation and Structures of Crystalline Aromatic Cation-Radical Salts. Triethyloxonium Hexachloroantimonate as a Novel (One-Electron) Oxidant. *J. Org. Chem.* **1998**, *63*, 5847−5856.

(46) Bell, F. A.; Ledwith, A.; Sherrington, D. C. Cation-Radicals: Tris(p-bromophenyl)amminium Perchlorate and Hexachloroantimonate. *J. Chem. Soc. C* **1969**, 2719−2720.

(47) Kim, E. K; Kochi, J. K. Charge-Transfer Structures of Aromatic Electron Donor-Acceptor Complexes Leading to Electron Transfer with the Electrophilic Nitrosonium Cation. *J. Am. Chem. Soc.* **1991**, *113*, 4962−4974.

(48) Barbosa, F.; Eberson, L.; Gescheidt, G.; Gronowitz, S.; Hörnfeldt, A.-B.; Juliá, L.; Persson, O. Structure of the Radicals Formed in Thermal and Photochemical Reactions of 3-Alkylthiophenes under Acidic Conditions. *Acta Chem. Scand.* **1998**, *52*, 1275−1284.

(49) Hill, M. G.; Penneau, J. F.; Zinger, B.; Mann, K. R.; Miller, L. L. Oligothiophene Cation Radicals. π-Dimers as Alternatives to Bipolarons in Oxidized Polythiophenes. *Chem. Mater.* **1992**, *4*, 1106−1113.

(50) We note that analyses of the spin densities using the NPA charges lead to very similar results. See the Appendix of the Supporting Information for more details.

(51) Lancaster, K.; Odom, S. A.; Jones, S. C.; Thayumanavan, S.; Marder, S. R.; Brédas, J. L.; Coropceanu, V.; Barlow, S. Intramolecular Electron-Transfer Rates in Mixed-Valence Triarylamines: Measurement by Variable-Temperature ESR Spectroscopy and Comparison with Optical Data. *J. Am. Chem. Soc.* **2009**, *131*, 1717−1723.